Journal of Engineering Mathematics **49:** 321–338, 2004.

Modelling of diffuse interfaces with temperature gradients

N. BESSONOV, J. A. POJMAN[1] and V. VOLPERT[2]
Institute of Problems of Mechanical Engineering, 199178 Saint Petersburg, Russia (E-mail: bessonov@ipme.ru); [1]*Department of Chemistry and Biochemistry, University of Southern Mississippi, Hattiesburg, MS 39406, USA (E-mail: john@pojman.com);* [2]*Laboratoire des Mathématiques Appliquées, UMR 5585 CNRS Université Lyon 1, 69622 Villeurbanne Cedex, France (E-mail: volpert@maply.univ-lyon1.fr)*

Received 27 June 2002; accepted in revised form 17 November 2003

Abstract. The work is devoted to capillary phenomena in miscible liquids under the assumption that they have a constant and the same density. The model consists of the heat equation, diffusion equation, and the Navier-Stokes equations with the Korteweg stress. We study several configurations corresponding to the microgravity experiments planned for the International Space Station. The basic conclusion of the numerical simulations is that transient capillary phenomena in miscible liquids exist and can produce convective flows sufficiently strong to be observed experimentally. In particular, there exists a miscible analogue to the Marangoni convection where the temperature gradient is applied along the transition zone between two fluids. Convection also appears if, instead of the temperature gradient, the case where the width of the transition zone varies in space is considered. Finally, similar to the immiscible case, miscible drops move in a temperature gradient.

Key words: diffuse interfaces, Korteweg stress, miscible liquids

1. Introduction

In this work we study transient interfacial phenomena in miscible liquids where a thermodynamically stable interface does not exist, and after some time the mixture becomes homogeneous in space due to diffusion. If the diffusion coefficient is sufficiently small, we can expect existence of interfacial phenomena, even if they are necessarily transient and depend on time.

This question was first discussed by Korteweg in 1901 [1] who introduced additional terms in the equations of motion to describe volume forces arising because of the long-range molecular interaction in liquids. In more recent works [2], [3] this type of model is derived by thermodynamical consideration under the assumption that the free energy depends on the square of the density or of the composition gradient.

To study the behavior of miscible liquids we use the model which consists of the Navier-Stokes equations with the Korteweg stress

$$\rho\left(\frac{\partial v_x}{\partial t}+v_x\frac{\partial v_x}{\partial x}+v_y\frac{\partial v_x}{\partial y}\right)=\frac{\partial}{\partial x}\left(S_{xx}+F_{xx}\right)+\frac{\partial}{\partial y}\left(S_{xy}+F_{xy}\right), \tag{1.1}$$

$$\rho\left(\frac{\partial v_y}{\partial t}+v_x\frac{\partial v_y}{\partial x}+v_y\frac{\partial v_y}{\partial y}\right)=\frac{\partial}{\partial x}\left(S_{yx}+F_{yx}\right)+\frac{\partial}{\partial y}\left(S_{yy}+F_{yy}\right) \tag{1.2}$$

and of the diffusion equation and heat equation with convective terms

$$\rho\left(\frac{\partial c}{\partial t}+v_x\frac{\partial c}{\partial x}+v_y\frac{\partial c}{\partial y}\right)=\nabla\cdot(d\nabla c), \tag{1.3}$$

$$\rho c_p \left(\frac{\partial T}{\partial t} + v_x \frac{\partial T}{\partial x} + v_y \frac{\partial T}{\partial y} \right) = \nabla \cdot (\lambda \nabla T), \tag{1.4}$$

where

$$S_{xx} = -p + 2\mu \frac{\partial v_x}{\partial x}, \quad S_{xy} = S_{yx} = \mu \left(\frac{\partial v_x}{\partial y} + \frac{\partial v_y}{\partial x} \right), \quad S_{yy} = -p + 2\mu \frac{\partial v_y}{\partial y}$$

are the components of the viscous stress tensor **S**,

$$F_{xx} = k \left(\frac{\partial c}{\partial y} \right)^2, \quad F_{xy} = F_{yx} = -k \frac{\partial c}{\partial x} \frac{\partial c}{\partial y}, \quad F_{yy} = k \left(\frac{\partial c}{\partial x} \right)^2$$

are the components of the Korteweg stress tensor **F**, v_x and v_y are the horizontal and the vertical components of the velocity, p is the pressure, ρ is the density, c_p the heat capacity, d the diffusion coefficient, λ is the thermal conductivity, T is the non-dimensional temperature, μ the dynamic viscosity, c the composition, *i.e.,* the function which changes between 0 and 1 such that $c = 0$ corresponds to one liquid and $c = 1$ to the other.

We assume in this work that the density is constant and consider the medium as incompressible,

$$\frac{\partial v_x}{\partial x} + \frac{\partial v_y}{\partial y} = 0. \tag{1.5}$$

The constant-density approximation will also allow us to study specifically the Korteweg stresses.

We consider the no-slip boundary conditions for the velocity,

$$v_x|_S = v_y|_S = 0 \tag{1.6}$$

and the no-flux boundary condition for the composition,

$$\left. \frac{\partial c}{\partial n} \right|_S = 0, \tag{1.7}$$

where S is boundary of the domain. The boundary condition for the temperature will be specified below.

The quantity k in the Korteweg stresses plays an important role in this theory. It is shown in [2] that it is determined by the free-energy-density dependence on the square of the density gradient. If we consider the case of a binary fluid with constant density but with a variable composition, as we do in this work, we can put (see [3])

$$k = \frac{\partial f(c, T, \alpha)}{\partial \alpha},$$

where $\alpha = |\nabla c|^2$. The temperature dependence of k couples the Equation (1.4) with the equations of motion (1.1), (1.2). We neglect the viscous heat dissipation in (1.4) since the fluid velocity is small.

Various questions related to the behavior of miscible liquids are studied experimentally and theoretically in [2]–[11]. The basic goal of this work is to study the influence of temperature gradients on diffuse interfaces in miscible liquids. As pointed out above, we assume that the

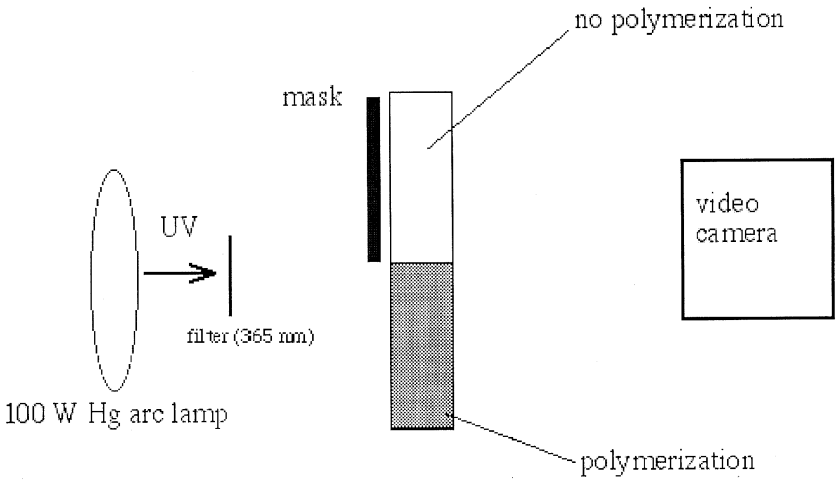

Figure 1. Experimental configuration.

density is constant and consider the case where the Korteweg parameter k or the diffusion coefficient d depend on the temperature. We will see that both of them can be at the origin of the effective interfacial tension in miscible liquids though in some cases they act differently. Finally, in view of the experiments proposed for the International Space Station, some of the simulations in this work are done with variable viscosity (see below).

2. Description of experiments

Transient Interfacial Phenomena in Miscible Polymer Systems (TIPMPS) is an investigation planned for the International Space Station to test how concentration and temperature gradients in a miscible polymer/monomer system can cause convection in the absence of buoyancy-driven convection.

A sharp transition zone between poly(dodecyl acrylate) and dodecyl acrylate, which are miscible, will be created by rapidly photopolymerizing dodecyl acrylate in a rectangular cuvette We will illuminate the reactor with 365 nm UV light, using masks that create a known interfacial profile between monomer and polymer. In some experiments a temperature gradient will be applied parallel to the transition zone. Figure 1 shows a schematic of the experimental set-up and how the mask produces two regions – one of unreacted monomer and one of hot polymer. The fluid flow will be measured by Particle Imaging Velocimetry (PIV). The temperature field will be measured with an array of thermistors, and the width of the transition zone will be measured optically.

In this work we model the proposed experiments where there is a temperature gradient along the transition zone or where the width of the transition zone varies in space. We will study also behavior of miscible drops in a temperature gradient.

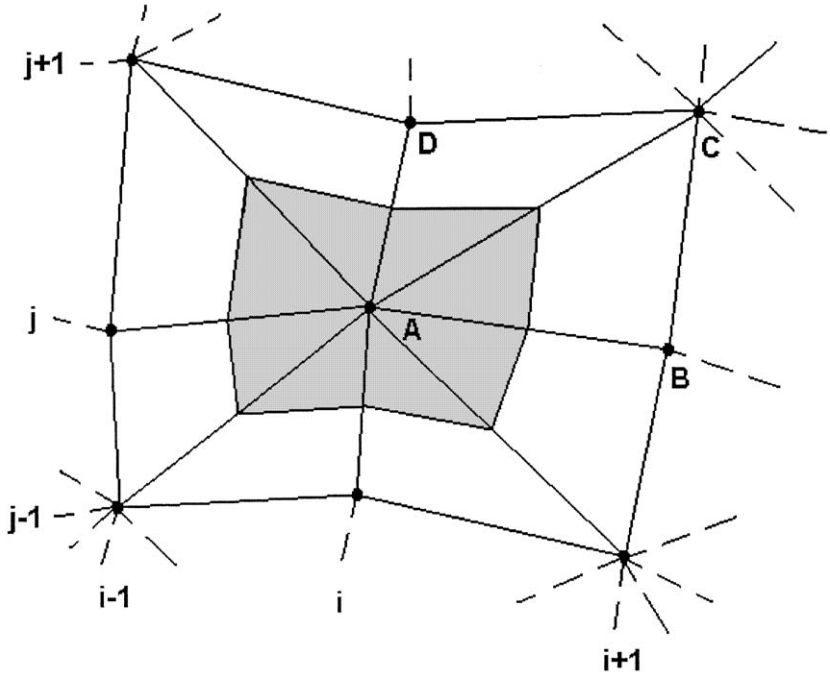

Figure 2. A fragment of the mesh. The control volume V_A is gray.

3. Numerical method

We rewrite the problem (1.1)–(1.5) in a coordinate-free form that is better adapted to describe the numerical method based on a Lagrangian mesh:

$$\rho\frac{\mathrm{d}\mathbf{v}}{\mathrm{d}t} = \nabla\cdot(\mathbf{S}+\mathbf{F}), \tag{3.1}$$

$$\rho\frac{\mathrm{d}c}{\mathrm{d}t} = \nabla\cdot(d\nabla c), \tag{3.2}$$

$$\rho c_p\frac{\mathrm{d}T}{\mathrm{d}t} = \nabla\cdot(\lambda\nabla T), \tag{3.3}$$

$$\nabla\cdot\mathbf{v} = 0, \tag{3.4}$$

where

$$\mathbf{S} = -p\mathbf{I} + \mu\left[\nabla\mathbf{v} + (\nabla\mathbf{v})^T\right],$$
$$\mathbf{F} = k\left[(\nabla c\cdot\nabla c)\mathbf{I} - \nabla c\nabla c\right],$$

$\mathbf{a}\cdot\mathbf{b}$ is the scalar product, $\mathbf{ab}$ is a dyadic product, $\mathbf{I}$ is the unit tensor, $\mathrm{d}\Phi/\mathrm{d}t \equiv \partial\Phi/\partial t + \nabla\cdot(\mathbf{v}\Phi)$.

For numerical simulations of the problem (3.1)–(3.4) we apply the finite-volume method. We use an adaptive nonorthogonal mesh $M \times N$ ($i = 1, ..., M,\ \ j = 1, ..., N$). Its fragment is shown in Figure 2. Each cell of the mesh (ABCD in Figure 2) consists of two triangular elements (ABC and ACD). The direction of the cell diagonal alternates in the neighboring cells.

The structure of the equations suggests to define the velocity, the composition, and the temperature at the nodes of the mesh (nodal variables), and the components of the stress tensors **S** and **F** are defined inside the triangular elements. Equation (3.4) is also solved at triangular elements.

For each node of the mesh we introduce a control volume as a polyderon with the sides passing through the middle points of the sides and diagonals of the cells. In Figure 2 the control volume V_A is shown for the node A.

We integrate the Equations (3.1)–(3.2) over each control volume. We have for the node A:

$$\rho\frac{\mathrm{d}}{\mathrm{d}t}\int_{V_A}\mathbf{v}\mathrm{d}V = \int_{S_A}\mathbf{n}\cdot\left\{-p\mathbf{I}+\mu\left[\nabla\mathbf{v}+(\nabla\mathbf{v})^T\right] + k\left[(\nabla c\cdot\nabla c)\mathbf{I}-\nabla c\nabla c\right]\right\}^{n+1}\mathrm{d}S, \tag{3.5}$$

$$\rho\frac{\mathrm{d}}{\mathrm{d}t}\int_{V_A}c\,\mathrm{d}V = \int_{S_A}d\mathbf{n}\cdot\nabla c^{n+1}\,\mathrm{d}S, \tag{3.6}$$

$$\rho\frac{\mathrm{d}}{\mathrm{d}t}\int_{V_A}c_pT\mathrm{d}V = \int_{S_A}\lambda\mathbf{n}\cdot\nabla T^{n+1}\,\mathrm{d}S, \tag{3.7}$$

where S_A is a boundary of a V_A, $\mathbf{n}$ is external normal to S_A, n is the number of the time step. Note that the flux terms in the right-hand sides of (3.5)–(3.7) are taken implicitly in time.

The left-hand sides of the Equations (3.5)–(3.7) are approximated as follows

$$\rho\frac{\mathrm{d}}{\mathrm{d}t}\int_{V_A}\mathbf{v}\,\mathrm{d}V = \rho\frac{\mathbf{v}_A^{n+1}-\mathbf{v}_A^n}{\Delta t}\sum_i V_i, \tag{3.8}$$

$$\rho\frac{\mathrm{d}}{\mathrm{d}t}\int_{V_A}c\,\mathrm{d}V = \rho\frac{c_A^{n+1}-c_A^n}{\Delta t}\sum_i V_i, \tag{3.9}$$

$$\rho\frac{\mathrm{d}}{\mathrm{d}t}\int_{V_A}c_pT\mathrm{d}V = \rho\frac{T_A^{n+1}-T_A^n}{\Delta t}\sum_i V_ic_{p_i}, \tag{3.10}$$

where $\sum_i$ is a sum over all triangles in the control volume V_A (obviously $\sum_i V_i \equiv V_A$).

The integrals in the right-hand sides of the Equations (3.5)–(3.7) are taken over the surfaces of control volumes. To compute these, we need to know the components of the stress tensors, and the components of the temperature and concentration gradients. In what follows we will use a discretization of ∇c, ∇T, $\nabla\cdot\mathbf{v}$, and $\nabla\mathbf{v}$ in triangular elements. For the sake of brevity we introduce the notation

$$\nabla\odot\Phi, \tag{3.11}$$

where Φ is scalar or vector nodal variable, $\odot$ denotes a distributive operation admissible for Φ. We use a linear interpolation of the nodal variable Φ inside each triangle ABC:

$$\Phi = \mathbf{A}\cdot\mathbf{r}+\mathbf{b}, \tag{3.12}$$

where $\mathbf{r} = \mathbf{i}_n x_n$, (summation convention over repeated subscripts is used), $\mathbf{b}$ is a constant tensor of the same rank as Φ, and the rank of $\mathbf{A}$ is one order higher. Substituting (3.12) in (3.11) gives

$$\nabla\odot\Phi = \mathbf{i}_n\odot\frac{\partial(\mathbf{A}\cdot\mathbf{i}_m x_m+\mathbf{b})}{\partial x_n} = \mathbf{i}_n\odot(\mathbf{A}\cdot\mathbf{i}_n). \tag{3.13}$$

For the vertices of the triangle ABC we can write

$$\begin{cases} \Phi_A = \mathbf{A}\cdot\mathbf{r}_A + \mathbf{b} \\ \Phi_B = \mathbf{A}\cdot\mathbf{r}_B + \mathbf{b} \\ \Phi_C = \mathbf{A}\cdot\mathbf{r}_C + \mathbf{b} \end{cases}, \tag{3.14}$$

or

$$\begin{cases} \Phi_1 = \mathbf{A}\cdot\mathbf{r}_1 \\ \Phi_2 = \mathbf{A}\cdot\mathbf{r}_2 \end{cases}, \tag{3.15}$$

where $\Phi_1 = \Phi_B - \Phi_A$, $\Phi_2 = \Phi_C - \Phi_A$, $\mathbf{r}_1 = \mathbf{r}_B - \mathbf{r}_A$, $\mathbf{r}_2 = \mathbf{r}_C - \mathbf{r}_A$. From (3.15) it follows that

$$\mathbf{A} = \Phi_m \mathbf{r}^m. \tag{3.16}$$

The vectors $\mathbf{r}_1, \mathbf{r}_2$ and $\mathbf{r}^1, \mathbf{r}^2$ are called reciprocal vectors. It is known that $\mathbf{r}_k \cdot \mathbf{r}^m = \delta_{km}$ and $\mathbf{r}_m\mathbf{r}^m = \mathbf{r}^m\mathbf{r}_m = \mathbf{I}$, where δ_{km} is the Kroneker delta symbol. For Cartesian coordinates $\mathbf{r}^1, \mathbf{r}^2$ can be written in the form

$$\mathbf{r}^1 = \frac{1}{D}\begin{vmatrix} \mathbf{i}_1 & \mathbf{i}_2 \\ r_{21} & r_{22} \end{vmatrix}, \quad \mathbf{r}^2 = \frac{1}{D}\begin{vmatrix} r_{11} & r_{12} \\ \mathbf{i}_1 & \mathbf{i}_2 \end{vmatrix}, \quad D = \begin{vmatrix} r_{11} & r_{12} \\ r_{21} & r_{22} \end{vmatrix}. \tag{3.17}$$

Substituting (3.16) in (3.13), we obtain

$$\nabla \odot \Phi = \mathbf{r}^m \odot \Phi_m, \tag{3.18}$$

or, explicitly

$$\nabla \odot \Phi = \mathbf{r}^1 \odot \Phi_1 + \mathbf{r}^2 \odot \Phi_2. \tag{3.19}$$

The discretization of $\nabla \odot \Phi$ in (3.19) given in the triangle ABC is a linear combination of the differences of its values at the vertices.

We note that (3.19) is a generalization of the simplest approximation

$$\nabla \odot \Phi = \mathbf{i}_1 \odot \frac{\Phi_B - \Phi_A}{\Delta x} + \mathbf{i}_2 \odot \frac{\Phi_C - \Phi_A}{\Delta y}, \tag{3.20}$$

written for the orthogonal mesh element on the nonorthogonal mesh element. Here $\Delta x = x_B - x_A$, $\Delta y = y_C - y_A$. We emphasize that similar to the case of the orthogonal mesh (3.20) the differences of nodal values in (3.19) are taken along the mesh lines. It will allow us to use for the nonorthogonal mesh practically the same algorithms as for the orthogonal mesh (see [12]).

Let us define the approximation of the integrals in the right-hand sides of the Equations (3.5)–(3.7) over the interval FE at the boundary S_A. The outward normal vector to it has the form

$$\mathbf{n} = \frac{\mathbf{r}^1}{|\mathbf{r}^1|}. \tag{3.21}$$

Using (3.19) and (3.21), we can obtain the difference approximation of the right-hand sides of the Equations (3.5)–(3.7) over FE. For example, we obtain the following approximation for (3.7):

$$\int_{FE} \lambda \mathbf{n}\cdot\nabla T \, \mathrm{d}S = \frac{1}{2}\lambda D \mathbf{r}^1 \cdot (\mathbf{r}^1 T_1 + \mathbf{r}^2 T_2). \tag{3.22}$$

Approximation of the integrals in right-hand sides of (3.5) and (3.6) can be obtained similarly.

Taking into account (3.18), we can represent the approximation of the continuity Equation (3.4) in the form

$$\nabla \cdot \mathbf{v} = \mathbf{r}^1 \cdot \mathbf{v}_1 + \mathbf{r}^2 \cdot \mathbf{v}_2, \tag{3.23}$$

where $\mathbf{v}_1 = \mathbf{v}_B - \mathbf{v}_A$, $\mathbf{v}_2 = \mathbf{v}_C - \mathbf{v}_A$.

To solve the discretized equations we use the iterative ADI method (see [13, Chapter 17]). Consider the difference equations approximating the system (3.5)–(3.7) in the form:

$$\Lambda(f) = 0, \tag{3.24}$$

where the difference operator Λ includes also the discretization of the time derivative, the components of the vector f includes $\mathbf{v}$, c, T and p. Suppose that the initial distribution for f is given. It can be the initial condition or the values at the previous time step.

The ADI method is based on the following iterative procedure. Let us introduce a parameter τ playing the role of pseudo-time in the iterations and denote by k the iteration number. We note that the number of iterations for a given time step n can be sufficiently large.

First of all we determine the residual $\widehat{f}^{\,k}$ at every node of the mesh,

$$\widehat{f}^{\,k} = \tau \Lambda(f^k). \tag{3.25}$$

For the boundary nodes $\widehat{f}^{\,k}$ is found from the boundary conditions. For example, the boundary condition $f = \text{const}$ implies $\widehat{f}^{\,k} = 0$.

We split Λ into two parts,

$$\Lambda = \Lambda_1 + \Lambda_2,$$

where Λ_1 contains a half of the expression in the left-hand sides of (3.5)–(3.7) and the integrals in the right-hand sides taken over the upper and the lower parts of the boundary S_A; Λ_2 also contains a half of the expression in the left-hand sides and the integrals taken over the lateral parts of the boundary.

The continuity equation can also be split in accordance with (3.23). At the following steps of the algorithm we find the iterations $\widehat{f}^{\,k+1/2}$ and $\widehat{f}^{\,k+1}$ from the equations

$$\frac{\widehat{f}^{\,k+1/2} - \widehat{f}^{\,k}}{\tau} = \Lambda_1\left(\widehat{f}^{\,k+1/2}\right), \tag{3.26}$$

$$\frac{\widehat{f}^{\,k+1} - \widehat{f}^{\,k+1/2}}{\tau} = \Lambda_2\left(\widehat{f}^{\,k+1}\right). \tag{3.27}$$

Finally we find f^{k+1}:

$$f^{k+1} = f^k + \widehat{f}^{\,k+1}. \tag{3.28}$$

We continue the iterations (3.25)–(3.28) while $\widehat{f}^{\,k}$ in (3.25) becomes sufficiently small.

We determine new positions of the nodes at each time step,

$$\mathbf{r}_A^{n+1} = \mathbf{r}_A^n + \Delta t \mathbf{v}_A^{n+1}. \tag{3.29}$$

If the flow leads to a strong deformation of the mesh, then it is reconstructed with the use of spline approximation for nodal and triangular variables. For the values of parameters used in

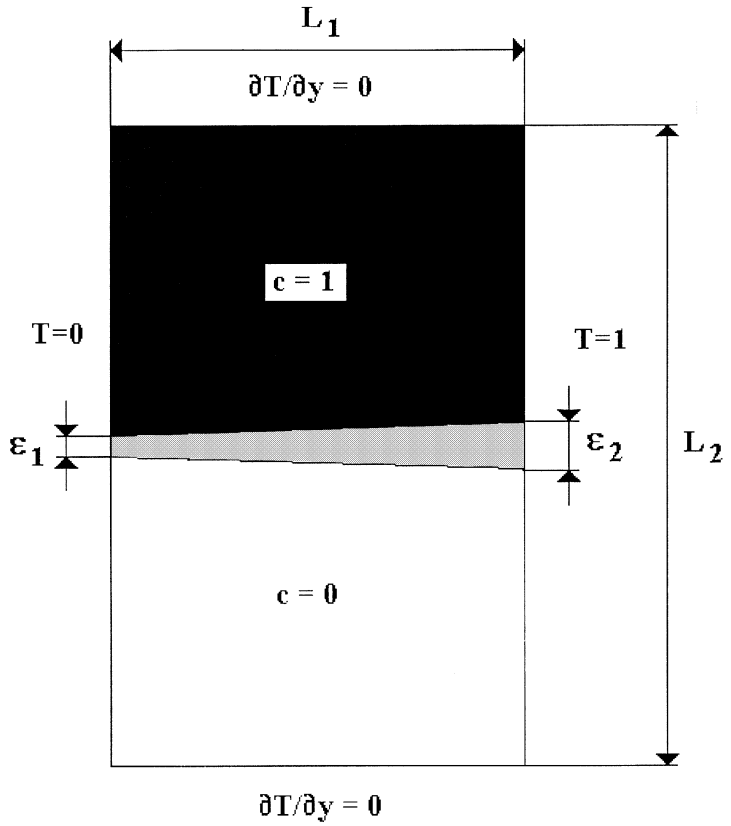

Figure 3. Computational domain and initial composition configuration.

these simulations the reconstruction of the mesh is usually done every several hundreds time steps.

4. Plane transition zone

In this section we discuss results of the numerical simulations of the system (3.1)–(3.4) in the rectangular domain $-L_x/2 \le x \le L_x/2$, $-L_y/2 \le y \le L_y/2$ with the plane transition zone $\epsilon = \epsilon_1 = \epsilon_2$ (Figure 3). We consider the no-slip boundary conditions for the velocity, and the no-flux boundary conditions for the concentration. The boundary conditions for the non-dimensional temperature are as follows:

$$\left.\frac{\partial T}{\partial y}\right|_{y=\pm L_y/2} = 0, \quad T|_{x=-L_x/2} = 0, \quad T|_{x=L_x/2} = 1. \tag{4.1}$$

The initial conditions model the situation where two miscible fluids are separated in space. The initial distribution of the composition is independent of x and it is a cubic polynomial across the transition zone,

$$c|_{t=0} = \begin{cases} 0, & \text{at } -L_y/2 \le y < -\varepsilon/2 \\ \dfrac{1}{2} + \dfrac{3}{4}\left(\dfrac{2y}{\varepsilon}\right) - \dfrac{1}{4}\left(\dfrac{2y}{\varepsilon}\right)^3, & \text{at } -\varepsilon/2 \le y < \varepsilon/2 \\ 1, & \text{at } \varepsilon/2 \le y \le L_y/2 \end{cases}. \tag{4.2}$$

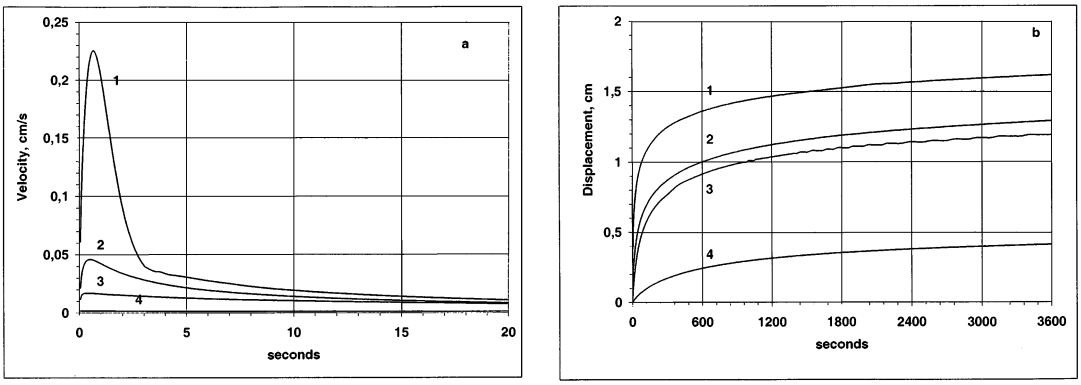

Figure 4. Maximal velocity (a) and maximal displacement (b), 1 - $\mu_0 = 0{\cdot}01$ Pa · s, $\sigma_c = 0$, 2 - $\mu_0 = 0{\cdot}1$ Pa · s, $\sigma_c = 0$, 3 - $\mu_0 = 0{\cdot}01$ Pa · s, $\sigma_c = 5$, 4 - $\mu_0 = 0{\cdot}1$ Pa · s, $\sigma_c = 5$.

The initial condition for the temperature T is a linear function depending on x only. Initially the liquid is unmovable, and the purpose of the simulations is to study convection induced by capillary forces in miscible liquids.

The viscosity dependence on the composition and on the temperature is approximated by the exponential

$$\mu(c, T) = \mu_0 \, \mathrm{e}^{\sigma_c c - \sigma_T T}, \tag{4.3}$$

$k(T)$ and $d(T)$ are considered as linear functions of T,

$$k(T) = k_0 - k_1 T, \quad d = d_0 + d_1 T. \tag{4.4}$$

Everywhere below we consider the values of parameters which correspond to the real experiments planned for the ISS: $L_x = 3$ cm, $L_y = 6$ cm, $\rho = 10^3$ kg/m^3, $\lambda = 0{\cdot}05$ W/(m · K), $c_p = 2 \times 10^3$ J/(kg · K). The values of the parameters are estimated experimentally. In particular, k_0 and k_1 are estimated by the spinning drop tensiometry. It is the experimentally observed effective interfacial tension for miscible liquids [9].

We will characterize convection by the maximal velocity at each moment of time and by the maximal displacement of a liquid particle. The second value is the most important for the experiments because it shows the experimental precision which is necessary to detect the convective motion.

To find the maximal displacement, we determine the displacement of each mesh node and then take the maximal among them.

4.1. k DEPENDS ON TEMPERATURE

In this subsection we consider the case where $k_0 = 2{\cdot}34 \times 10^{-6}$ N, $k_1 = 1{\cdot}26 \times 10^{-6}$ N, $\sigma_T = 0$, $d_0 = 2{\cdot}5 \times 10^{-5}$ kg/(m · s), $d_1 = 0$.

Results of the calculations of the maximum of velocity $V_{\max}$ as functions of μ_0, σ_c and ε is shown in Tables 1, 2 and Figure 4 (for the same values of parameters as in Table 1).

Figures 4a, 4b show the maximal velocity and the maximal displacement, respectively, for the specific values of the parameters μ_0 and σ_c. In all cases the maximal velocity is reached during the first several seconds and after that it decreases rapidly in the beginning and slowly later. As we can expect, the velocity is greater for the less viscous liquid. Curve

Table 1. $V_{\max}$ (cm/s), $\varepsilon = 1{\cdot}8$ mm.

μ_0, (Pa · s)	σ_c					
	0	1	2	3	4	5
0·01	0·224	0·164	0·106	0·0585	0·0313	0·0169
0·025	0·132	0·0883	0·0509	0·0261	0·0133	0·00704
0·05	0·0809	0·0505	0·0275	0·0137	0·00684	0·00359
0·075	0·0584	0·0354	0·0189	0·00928	0·00461	0·00241
0·1	0·0457	0·0273	0·0144	0·00703	0·00348	0·00182

Table 2. $V_{\max}$ (cm/s), $\varepsilon = 0{\cdot}9$ mm.

μ_0, (Pa · s)	σ_c					
	0	1	2	3	4	5
0·01	0·365	0·272	0·177	0·0969	0·0487	0·024
0·025	0·224	0·153	0·0884	0·0441	0·0209	0·01
0·05	0·142	0·0905	0·0489	0·0234	0·0108	0·00513
0·075	0·105	0·0647	0·034	0·016	0·00731	0·00345
0·1	0·0831	0·0504	0·0261	0·0122	0·00554	0·0026

1 corresponds to the minimal and curve 4 to the maximal viscosity (see (4.3)). The value of μ_0 is 10 times more for curve 2 than for curve 3. However, the maximal velocity for the second case is essentially greater. It results from the difference of values of σ_c. The viscosity in the transition zone grows in the third case and slows down the convective motion due to the effective interfacial tension. The displacement is maximal in the case $\mu_0 = 0{\cdot}01$, $\sigma_c = 0$ (curve 1) and minimal for $\mu_0 = 0{\cdot}1$, $\sigma_c = 5$ (curve 4, Figure 4b). The distance between curves 2 and 3 remains practically constant after the initial period of the simulations. The displacement growth is fast in the beginning and it slows down in time because the driving force decreases due to diffusion. After the first 10 minutes it reaches about 75% of its value observed after 60 minutes. In the most realistic case $\mu_0 = 0{\cdot}01$, $\sigma_c = 5$ (curve 3) it is about 1 cm, and it should be possible to observe it experimentally.

The velocity field and the numerical mesh (with each second mesh line) are shown in Figure 5. There is one vortex from each side of the transition zone with the upper vortex being essentially weaker than the lower one because of the viscosity dependence on c. The deformation of the numerical mesh in the lower part of the domain is stronger than in the upper part because the fluid velocity there is larger (Figure 5b). The liquid motion along the central line is directed from the side with a higher temperature to the side with a lower temperature. This corresponds to the decrease of the effective interfacial tension due to the temperature dependence $k(T)$. We note that the vortex in the upper part of the domain where the liquid is more viscous increases in time while the vortex in the less viscous liquid decreases.

Isolines of the temperature (“vertical” lines) and of the composition (“horizontal” lines) are shown in Figure 6. The isotherms change in time being more curved in about 50–100 seconds because of the convection (Figures 6a,b). The temperature distribution becomes more close

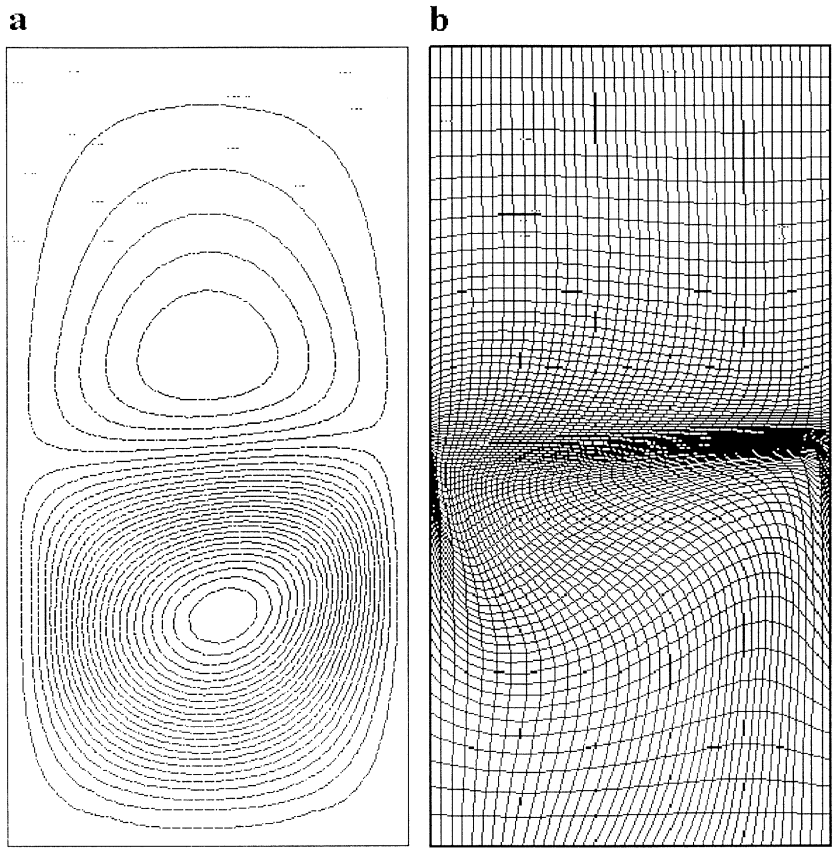

Figure 5. Stream function (a) and numerical mesh (b) after 1000 s; $k_0 = 1{\cdot}17 \times 10^{-6}$ N, $k_1 = 0{\cdot}63 \times 10^{-6}$ N, $\mu_0 = 0{\cdot}01$ Pa · s, $\sigma_c = 5$, $\sigma_T = 0$, $d_0 = 2{\cdot}5 \times 10^{-5}$ kg/(m · s), $d_1 = 0$.

to a linear one for large time (Figure 6c). Finally the isolines of the concentration show that the transition zone is larger in the left part of the domain where the vortices are directed from the central part outside, and it is narrower in the right part of the domain where the diffusion is upwind. Therefore the change in the width of the transition zone due to the convection acts to compensate the difference in the effective interfacial tension related to the nonuniform temperature distribution.

This means that not only diffusion decreases the interfacial tension in miscible liquids but also convection. In about 10 hours of the physical time the system practically reaches the steady state where the temperature distribution is linear, the composition distribution is uniform in space, and the liquid velocity is zero.

If we decrease the initial width of the transition zone and at the same time decrease proportionally $k(T)$, we can expect that the behavior of the system will be the same because the effective interfacial tension can be estimated as $k(T)/\delta$. However, the numerical simulations show that the maximal velocity and displacement are essentially less in this case. A possible explanation of this effect is connected with the influence of diffusion. If the width of the transition zone is less, *i.e.*, the composition gradients are greater, diffusion will be also faster and the effective interfacial tension will decrease more rapidly. Decreasing the diffusion coefficient, we obtain greater values of the velocity and of the displacement.

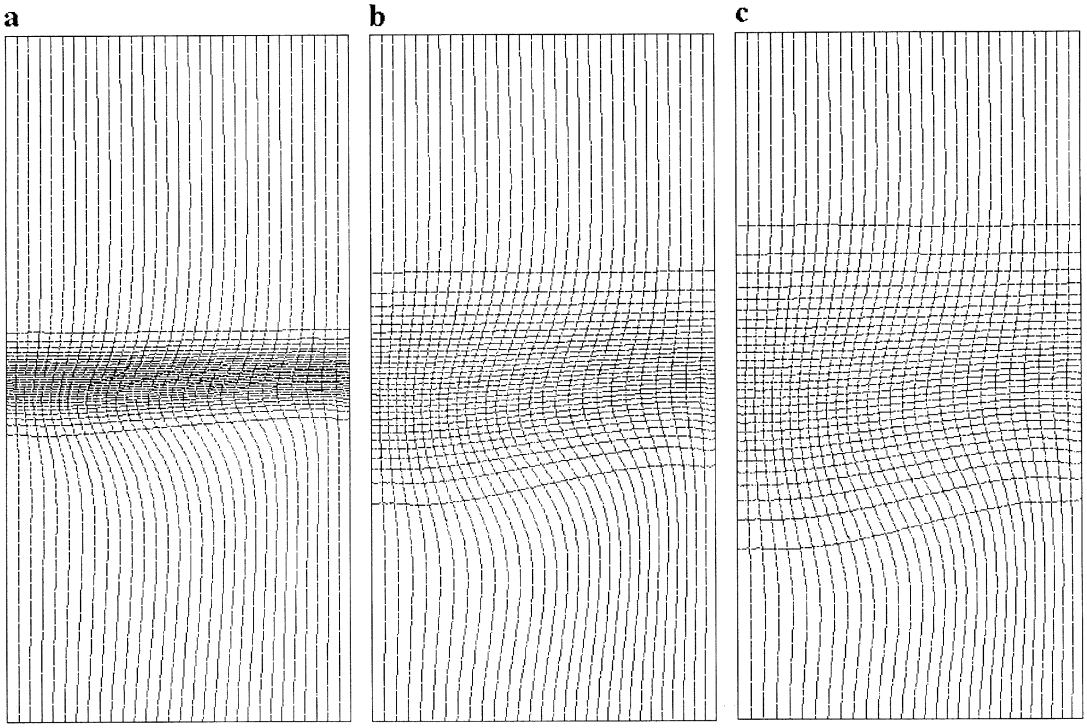

Figure 6. Isolines of the temperature ("vertical") and of the composition ("horizontal"), a - 100 s, b - 500 s, c - 1000 s (the same values of parameters as for Figure 5).

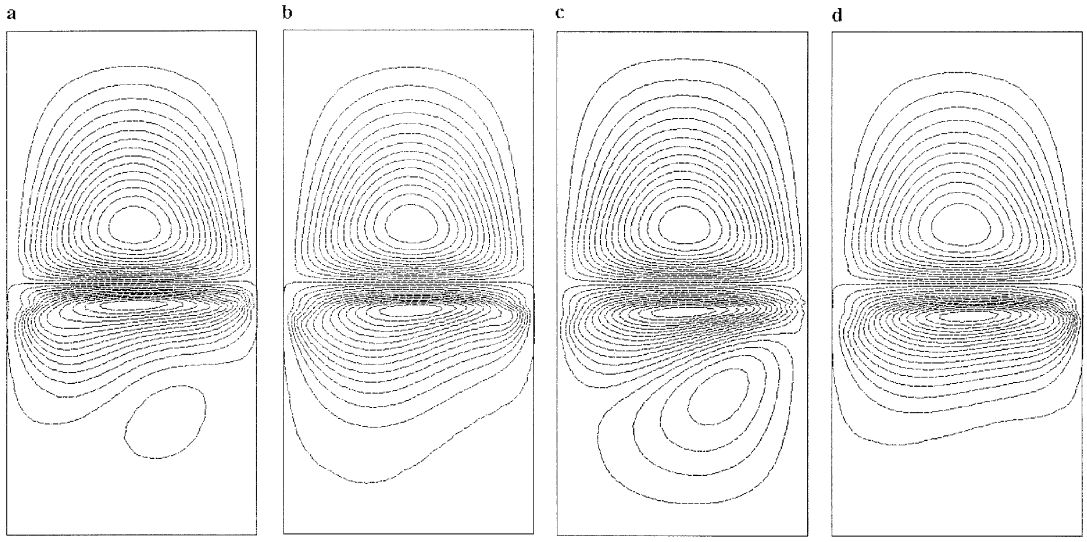

Figure 7. Level lines of the stream function for the oscillating regime, a - 7000 s, b - 9000 s, c - 11000 s, d - 13000 s; $k_0 = 0{\cdot}975 \times 10^{-6}$ N, $k_1 = 0{\cdot}125 \times 10^{-6}$ N, $\mu_0 = 0{\cdot}01$ Pa · s, $\sigma_c = 5$, $\sigma_T = 0$, $d_0 = 10^{-7}$ kg/(m · s), $d_1 = 0$.

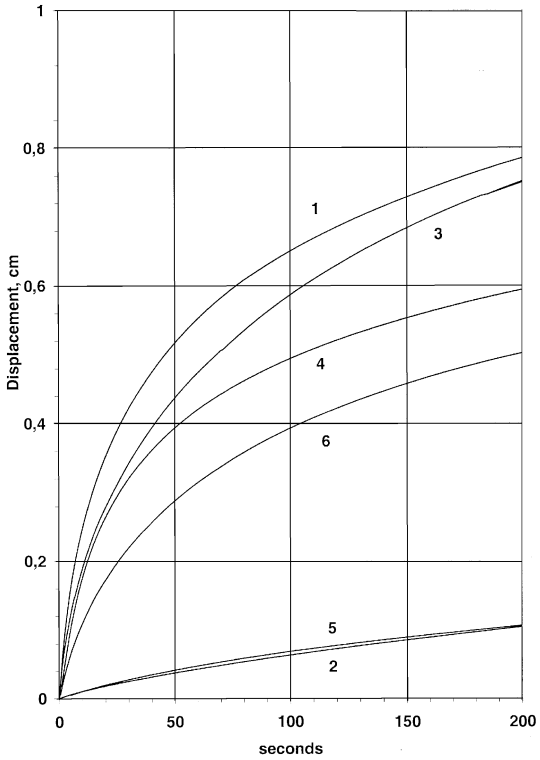

Figure 8. Comparison of the maximal displacement for $k(T)$ and $d(T)$; $k_0 = 1{\cdot}3 \times 10^{-6}$ N, $\mu_0 = 0{\cdot}1$ Pa · s, $d_0 = 10^{-5}$ kg/(m · s), 1 - $k_1 = 0{\cdot}7 \times 10^{-6}$ N, $\sigma_c = 0$, $\sigma_T = 0$, $d_1 = 0$, 2 - $k_1 = 0{\cdot}7 \times 10^{-6}$ N, $\sigma_c = 5$, $\sigma_T = 0$, $d_1 = 0$, 3 - $k_1 = 0{\cdot}7 \times 10^{-6}$ N, $\sigma_c = 5$, $\sigma_T = 5$, $d_1 = 0$, 4 - $k_1 = 0{\cdot}7 \times 10^{-6}$ N, $\sigma_c = 0$, $\sigma_T = 0$, $d_1 = 4 \times 10^{-5}$ kg/(m · s), 5 - $k_1 = 0{\cdot}7 \times 10^{-6}$ N, $\sigma_c = 5$, $\sigma_T = 0$, $d_1 = 4 \times 10^{-5}$ kg/(m · s), 6 - $k_1 = 0{\cdot}7 \times 10^{-6}$ N, $\sigma_c = 5$, $\sigma_T = 5$, $d_1 = 4 \times 10^{-5}$ kg/(m · s).

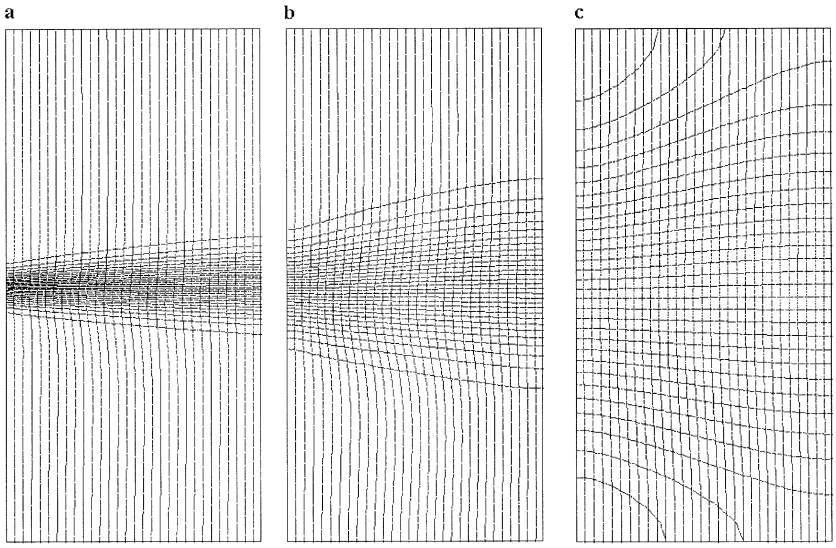

Figure 9. Isolines of the temperature ("vertical") and of the composition ("horizontal") in the case of the temperature dependent diffusion coefficient, a - 100 s, b - 500 s, c - 5000 s; $k_0 = 1{\cdot}3 \times 10^{-6}$ N, $k_1 = 0$, $\mu_0 = 0{\cdot}1$ Pa · s, $\sigma_c = 5$, $\sigma_T = 0$, $d_0 = 10^{-5}$ kg/(m · s), $d_1 = 4 \times 10^{-5}$ kg/(m · s).

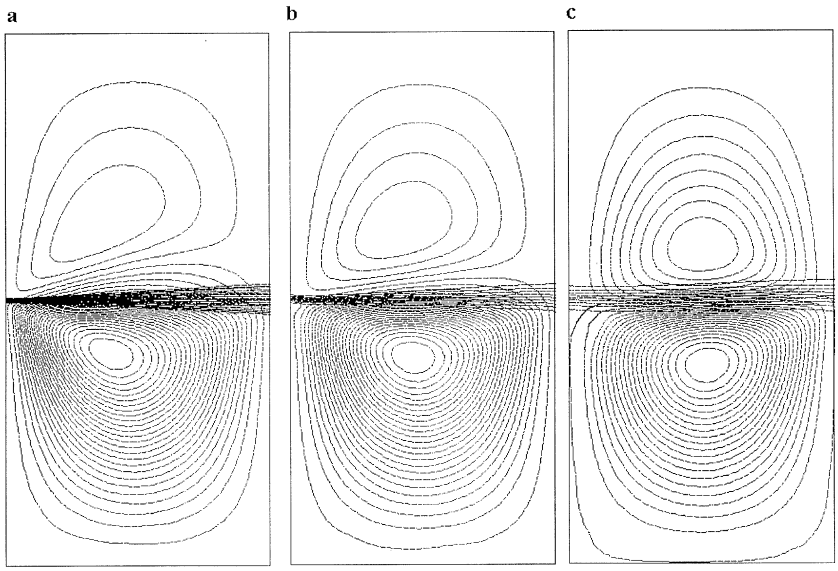

Figure 10. Level lines of the composition and of the stream function in the isothermal case with a variable transition zone, a - 1 s, b - 500 s, c - 5000 s; $\epsilon_1 = 0{\cdot}2$mm, $\epsilon_2 = 5$mm, $k_0 = 1{\cdot}95 \times 10^{-9}$ N, $k_1 = 0$, $\mu_0 = 0{\cdot}002$ Pa · s, $\sigma_c = 5$, $\sigma_T = 0$, $d_0 = 10^{-7}$ kg/(m · s), $d_1 = 0$.

4.2. OSCILLATIONS

For larger values of k than were considered in the previous subsection the qualitative behavior of the system can be different. The vortex in the lower part of the reactor, where the liquid is less viscous becomes stronger and leads to appearance of a counter vortex (Figure 7a). It becomes stronger with time while the intermediate vortex weakens. Therefore, the compensating action of convection also weakens. After some time the difference in the effective interfacial tension at the left and at the right increases again, resulting in a subsequent increase of the convective motion near the interface. The intermediate vortex increases eliminating the new vortex. This is a possible physical mechanism of the oscillations observed numerically (Figures 7a–d). The oscillations are decaying since the effective interfacial tension decreases due to diffusion.

4.3. d DEPENDS ON TEMPERATURE

In the previous subsection we have studied the case where the Korteweg coefficient is temperature dependent while the diffusion coefficient is constant. As we have already discussed in the introduction, there are two possible mechanisms how the effective interfacial tension in miscible liquids with a constant density can depend on the temperature: through the temperature dependence of k or through the temperature dependence of d. The experimental investigation of the dependence $k(T)$ appears to be very difficult and the results are not well reproducible because of the transient character of these phenomena. On the other hand, the temperature dependence of the diffusion coefficient is easier to measure. In this subsection we study the model (3.1)–(3.4) with a constant k and with the diffusion coefficient depending on the temperature.

We note first of all that the qualitative behavior of the maximal displacement and of the maximal velocity in time is the same as described in Section 4.1 (Figure 8). The flow at the

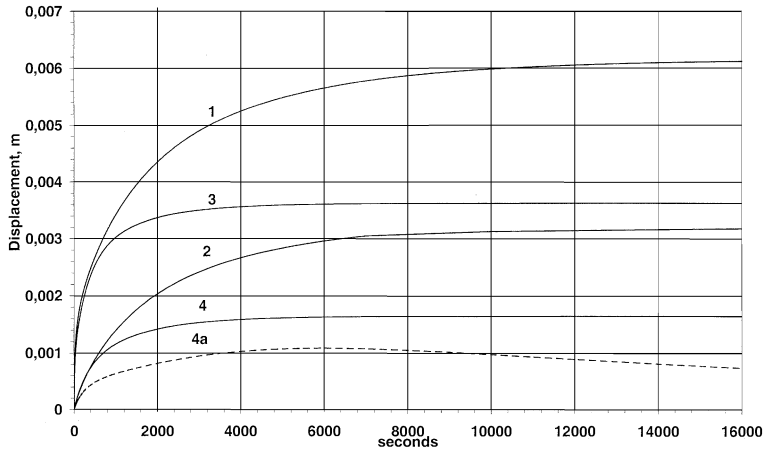

Figure 11. Displacement of the drop; $k_0 = 1{\cdot}3 \times 10^{-6}$ N, $\mu_0 = 0{\cdot}1$ Pa · s, $\sigma_T = 0$, $d_0 = 10^{-5}$ kg/(m · s). Position of the central node in time, 1 - $k_1 = 0{\cdot}7 \times 10^{-6}$ N, $\sigma_c = 0$, $d_1 = 0$, 2 - $k_1 = 0{\cdot}7 \times 10^{-6}$ N, $\sigma_c = 5$, $d_1 = 0$, 3 - $k_1 = 0$, $\sigma_c = 0$, $d_1 = 4 \times 10^{-5}$ kg/(m · s), 4 - $k_1 = 0$, $\sigma_c = 5$, $d_1 = 4 \times 10^{-5}$ kg/(m · s), 4a - Position of the center of mass in time (for the same parameters as 4).

transition zone is directed from the right where the temperature is greater to the left where it is less. It is related to the fact that the diffusion coefficient increases with the temperature, and the width of the transition zone is greater near the right wall than near the left one (Figure 9) contrary to what we have seen before (*cf.* Figure 6). Therefore there exists a force directed along the interface from the right to the left.

The width of the transition zone can be roughly estimated as $\sqrt{dt}$, where d is the diffusion coefficient and t time. Therefore the effective interfacial tension is proportional to $k/(\sqrt{dt})$. Thus if the change of $k(T)$ when we change T from the minimal to the maximal value is the same as the change of $\sqrt{d(T)}$, we can expect that the results are close. We compare the results in Figure 8. Curves 2 and 5 are really close to each other, while the difference in curve 1 and 4, 3 and 6 is larger but still they give a reasonable agreement taking into account that the arguments above are only qualitative.

Thus, in both cases where one of the coefficients k and d is temperature dependent and another one is constant, the convection appears in the initially unmovable medium. The flow patterns are rather similar qualitatively and even quantitatively.

5. Other configurations

5.1. Variable transition zone

In this section we model another experimental configuration. The system is isothermal, and the width of the transition zone between two liquids varies in space. It equals ϵ_1 from the left, ϵ_2 from the right, and it changes linearly as a function of x (see Figure 3).

The qualitative behavior of the system is the same as before. The effective interfacial tension directed along the transition zone creates a convective motion.

Figure 10 shows the evolution of the composition and of the stream function. Initially the width of the transition zone increases linearly from the left to the right.

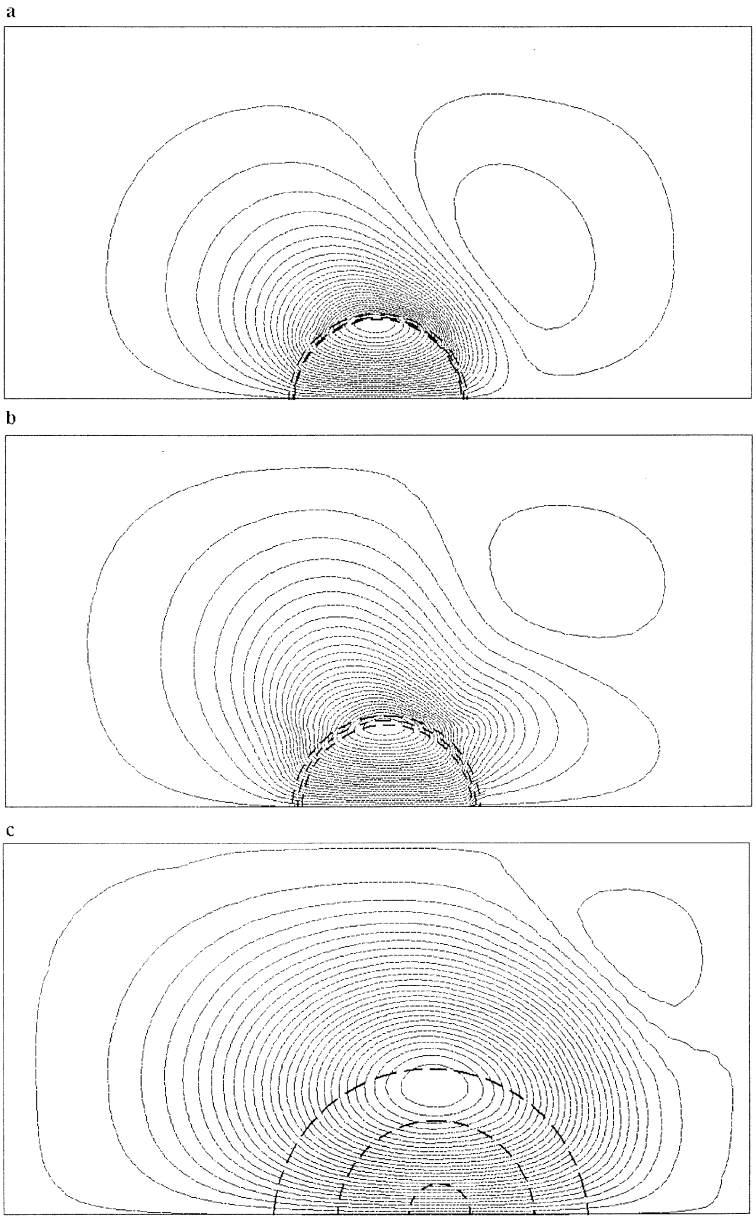

Figure 12. Evolution of the level lines of the stream function for the moving drop (upper half-drop), a - 2 s, b - 20 s, c - 2000 s; dashed lines - level lines of the composition $c = 0{\cdot}1$, $c = 0{\cdot}2$, $c = 0{\cdot}3$; $k_0 = 1{\cdot}3 \times 10^{-6}$ N, $k_1 = 0{\cdot}7 \times 10^{-6}$ N, $\mu_0 = 0{\cdot}1$ Pa · s, $\sigma_c = 5$, $\sigma_T = 5$, $d_0 = 10^{-5}$ kg/(m · s), $d_1 = 0$.

After some time the convection makes it practically the same from both sides of the reactor though the transition zone is slightly curved. In 10 hours the velocity decrease is about four orders of magnitude and the composition distribution becomes almost uniform.

It is interesting to note that a ten-fold increase of the Korteweg coefficient changes the final displacement by a factor of about two.

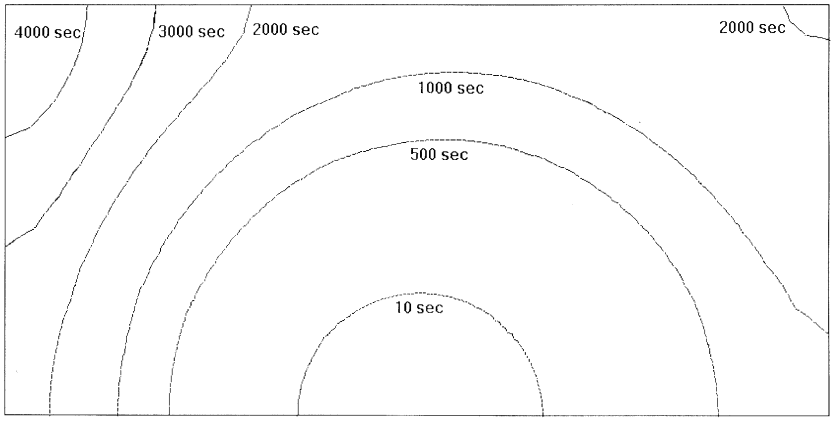

Figure 13. Evolution of the level line $c = 0{\cdot}01$ of the composition (the same values of parameters as in Figure 12).

5.2. MOTION OF DROPS

In this section we discuss the behavior of miscible drops in a temperature gradient. In the case of immiscible liquids a drop moves in the temperature gradient to the place where the temperature is greater. It appears that the behavior of miscible drops is qualitatively the same. Figure 11 shows the motion of the drop in time where we plot the coordinate of the central node of the drop (curves 1–4) or the center of mass (curve 4a). The displacement is larger in the case of a constant viscosity. In the case $\sigma_c = 5$ the liquid inside the drop is more viscous than the surrounding liquid, and it slows down the convective motion. The motion of the drop itself also slows down.

We note that the central node of the drop moves monotonically from the left to the right and practically stops for $t > 8000$ s when the drop is basically dissolved, and the effective interfacial tension becomes negligible. At the same time the center of mass begins to move backwards because it should return to the center of the domain when the composition distribution becomes homogeneous in space.

The flow pattern is shown in Figure 12. We note that the pressure inside the drop is practically constant and is essentially higher than outside of the drop. Therefore there is a pressure jump at the transition zone; this fact known for immiscible drops and predicted in [2] for miscible drops. The drop diffuses (Figure 13), and after some time the concentration distribution becomes homogeneous in space.

6. Concluding remarks

In this work we study theoretically behavior of miscible liquids in order to show that there exists an effective interfacial tension between them. If initially the liquids are separated in space, then a diffuse interface separating them exists though its width grows with time. At the first stage of the process where the concentration gradients are sufficiently high, we can expect a behavior similar to that for immiscible liquids.

Numerical simulations based on the model that includes the heat equation and the diffusion equation with convective terms, and the Navier-Stokes equations with the Korteweg stress are carried out for several configurations corresponding to microgravity experiments planned for the International Space Station with realistic values for the essential parameters. In particular,

if a temperature gradient is applied along the diffuse interface, then a convective motion in the initially unmovable medium appears similar to the surface tension induced convection well known in the immiscible case. According to the numerical results this convection can be observed experimentally.

We also simulate a miscible drop in a temperature gradient and show that a drop will migrate as an immiscible is known to do.

Future work includes studying how gradients in concentration along the diffuse interface and how variations in the width of the interface can cause convection.

References

1. D.J. Korteweg, Sur la forme que prennent les équations du mouvement des fluides si l'on tient compte des forces capillaires causées par des variations de densité considérables mais connues et sur la théorie de la capillarité dans l'hypothèse d'une variation continue de la densité. *Archives Néerlandaises des Sciences Exactes et Naturelles* 6 (1901) 1–24.
2. L.K. Antanovskii, Microscale theory of surface tension. *Physical Review E*, 54 (1996), 6285–6290.
3. D.M. Anderson, G.B. McFadden and A.A. Wheeler, Diffuse interface methods in fluid mechanics. *Ann. Rev. Fluid Mech.* 30 (1998) 139–165.
4. D. Jacqmin, Contact-line dynamics of a diffuse fluid interface. *J. Fluid Mech.* 402 (2000) 57–88.
5. D.D. Joseph and Y.Y. Renardy, *Fundamentals of Two-Fluid Dynamics.* Part II, Lubricated transport, drops and miscible fluids. New-York: Springer (1992).
6. P. Petitjeans, Une tension de surface pour les fluides miscibles. *C.R. Acad. Sci. Paris, Série II b* 322 (1996) 673–679.
7. P. Petitjeans, Fluides non miscible/fluides miscibles: des similitudes intéressantes. *C.R. Acad. Sci. Paris, Série II b* 325 (1997) 587–592.
8. J. Pojman, R. Texier and V. Volpert, Convection induced by composition gradients in miscible systems. *C.R. Acad. Sci. Paris, Mécanique,* 330 (2002) 353–358.
9. J. Pojman, N. Bessonov, R. Texier, V. Volpert and H. Wilke, Numerical simulations of transient interfacial phenomena in miscible fluids. AIAA 2002-0892, 40th Aerospace Sciences Meeting, Reno (2002).
10. I. Rousar and E.B. Nauman, A continuum analysis of surface tension in nonequilibrium systems. *Chem. Eng. Comm.* 129 (1994) 19–28.
11. Y.B. Zeldovich, About surface tension of a boundary between two mutually soluble liquids. *Zhur. Fiz. Khim.* 23 (in Russian) (1949) 931–935.
12. N.M. Bessonov and D.J. Song, Application of vector calculus to numerical simulations of continuous mechanics problems. *J. Comp. Phys.* 167 (2001) 22–38.
13. C. Hirsch, *Numerical Computation of Internal and External Flows.* Vol. 2. New York: Wiley (1988) 685 pp.